ACS APPLIED MATERIALS & INTERFACES

Research Article

www.acsami.org

Ultrafine ZnO Nanoparticles/Nanowires Synthesized on a Flexible and Transparent Substrate: Formation, Water Molecules, and Surface Defect Effects

Jyh Ming Wu,*[,†] Yi-Ru Chen,[‡] and Wei Tsung Kao[‡]

[†]Department of Material Science and Engineering, National Tsing Hua University, 101, Section 2 Kuang Fu Road, Hsinchu 300, Taiwan

[‡]Department of Materials Science and Engineering, Feng Chia University, 100 Wenhwa Road, Seatwen, Taichung 40724, Taiwan

ABSTRACT: The ultrafine ZnO nanoparticles/nanowires were successfully synthesized on a flexible and transparent substrate by an ultraviolet-light decomposition process. We demonstrate that water molecules can affect the morphology of ZnO nanostructures. An ultraviolet lamp ($\lambda \sim 380$ nm, 75 mW cm^{-2}) can be used to irradiate $Zn(AcAc)_2$ and $Zn(AcAc)_2{\cdot}H_2O$ precursors, which rapidly synthesize ZnO nanoparticles and nanowires, respectively. High-resolution transmission electron microscopy (HRTEM) images and a selected-area electron diffraction pattern revealed that the single-crystal nanoparticles were comprised of wurtzite structure ZnO. The nanowires consisted of ultrafine nanoparticles. On the basis of the Debye−Scherrer formula, the particle size of ZnO was calculated as ∼6−9 nm. The more water molecules the precursor had, the more OH^- and $Zn[(OH)_4]^{2-}$ it put out. Moreover, due to the $Zn[(OH)_4]^{2-}$ and $Zn(OH)_2$ species formed on the surface of the ZnO nanocrystals, they facilitated the one-dimensional nanowires during the crystal growth process. On the basis of our investigations, oxygen vacancies, hydroxyl, and zinc hydroxide all acted as key components in the formation processes that determined photoresponsive properties.

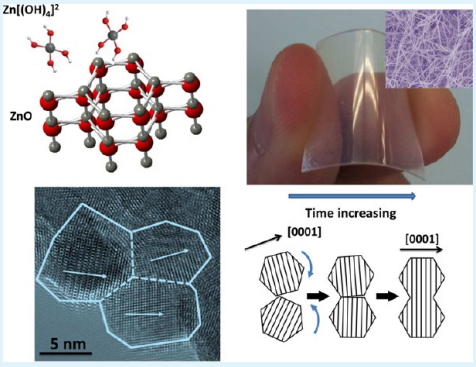

KEYWORDS: *ZnO, nanoparticles, nanowires, flexible, transparent, ultraviolet light*

1. INTRODUCTION

Zinc oxide (ZnO) nanostructures have shown promise for commercial applications in nanosensors,[1−3] photovoltaic cells,[4] nanogenerators,[5] and photocatalysis.[6] Many reports have described syntheses of ZnO nanowires through demonstrating various chemical processes that are simple and may also have industrial applications. In our previous works,[7] an ultraviolet decomposition method with a short processing time (i.e., ∼5 min) was successfully developed for the synthesis of ZnO nanowires under an ambient air.[8] These prior works found the zinc hydroxide (i.e., $Zn(OH)_2$) species acted as a key component that determined photocatalytic activities.[7,8] We revealed that the $Zn(OH)_2$ formed a larger number of surface defect states on the surface of the ZnO nanocrystals during the formation process.

In this work, a UV-light decomposition process has been successfully developed to deposit the nanowires/nanoparticles on a flexible substrate made of polyethylene terephthalate (PET) with a high transparency. To study the influence of the ZnO nanocrystals' formation process and their photoresponsive properties, a comprehensive experimental investigation was performed to address the water molecules and surface defect effect as raised from $Zn(OH)_2$. Isopropylalcohol (IPA) solvents with and without added water were mixed with zinc acetylacetonate hydrate powder to prepare $Zn(AcAc)_2$ and $Zn(AcAc)_2{\cdot}H_2O$ precursors; these were marked as precursors A and B, respectively. After being irradiated with UV-light ($\lambda \sim$ 360−380 nm), the precursors A and B were decomposed into zero-dimensional (0D) ultrafine nanoparticles and one-dimensional (1D) nanowires, respectively. The nanowires consisted of ultrafine nanoparticles that were ∼6−9 nm wide according to the Debye−Scherrer formula and HRTEM images evaluation. The ZnO nanoparticles exhibited a remarkable photocurrent−dark-current ratio of ∼80 900%, which is 8.5 times that of the ZnO nanowires (9000%).[8] Through our investigation, we determined that water molecules and surface defect states (i.e., oxygen vacancies ($V_o^{\cdot\cdot}$) and zinc interstitial vacancies (Zn_i^{2+})) raised from hydroxyl and zinc hydroxide acted as a key component in the crystal growth and photoresponsive process, respectively. Therefore, not only did zinc hydroxide affect the chemical reaction but also water molecules played a critical role during the formation process. We suggested that water molecules exhibited a ligand exchange reaction between the $AcAc^-$ and OH^- in the $Zn(AcAc)_2$-containing solution when water was added into the precursor of $Zn(AcAc)_2$.[9] The high concentration of hydroxyl ions and H_2O in the precursor

Received: October 15, 2013
Accepted: November 27, 2013
Published: November 27, 2013

provided plenty of opportunities to make Zn^{2+} react with OH^- to form $Zn[(OH)_4]^{2-}$ in facilitating one-dimensional nanowires.[8,10,11]

Utilizing transmission electron microscopy (TEM), X-ray photoelectron spectroscopy (XPS), and cathodoluminescence (CL) spectra investigations, it was discovered that, during the decomposition process, the ZnO nanowires displayed many surface features, such as oxygen vacancies, interstitial Zn, and zinc hydroxide. Water molecules were found to play a critical role in the surface defect states and to affect the morphology and the photoresponsive properties of the nanoparticles/nanowires.

2. EXPERIMENTAL SECTION

To determine the influence of water molecules on the formation mechanism of the nanowires, a zinc acetylacetonate hydrate solute was added to 2 mL of isopropyl alcohol without deionized water (DI) solvent to prepare $Zn(AcAc)_2$ precursors, which were marked as A-series samples. A control sample group of $Zn(AcAc)_2$ precursors with DI water were marked as B-series samples. The as-prepared precursors were then spray coated (at 25 °C) on flexible polyethylene terephthalate (PET) substrates under ambient air. After coating, the substrates were then subjected to UV-decomposition for 3−30 min to synthesize the ZnO nanoparticles/nanowires.

The structures of the samples were assessed by a thin-film X-ray diffractometer (XRD, Bruker). Measurements of morphology and crystal structure were obtained with field emission scanning electron microscopy (FESEM, HITACHI, S-4800) and high-resolution transmission electron microscopy (HRTEM, JEOL, JEM-3000F). A cathodoluminescence detector (Mono CL, Gatan) installed in the FESEM was used to investigate the luminescent properties of ZnO nanowires/nanoparticles. The chemical nature of the ZnO nanowires was evaluated by high-resolution X-ray photoelectron spectroscopy (HRXPS, ULVAC-PHI, AES 650) using monoaluminum. UV-light ($\lambda \sim 365$ nm, $I = 76$ mW/cm^2) was used to decompose the $Zn(AcAc)_2$ and $Zn(AcAc)_2H_2O$ precursors. As-synthesized nanowires/nanoparticles were characterized by Fourier transform infrared spectroscopy (FTIR) to investigate their surface compositional properties. In addition, UV-light ($\lambda \sim 365$ nm, $I = 2.34$ mW/cm^2) acted as the excitation source during photoelectric current measurements that investigated the UV-sensing properties of as-synthesized ZnO nanoparticles/nanowires.[12]

3. RESULTS AND DISCUSSION

Figure 1(a) shows that the ZnO nanoparticles were synthesized from precursors A, with a 5 min UV-decomposition process. The resulting nanoparticles and nanowires were therefore named samples A and B, respectively. Figure 1(a) and its inset image shows that the FESEM for sample A exhibited a 0D nanoparticle. The corresponding TEM images of Figures 1(b) and 1(c) show that the size of the nanoparticle was ∼5−10 nm with lattice fringes of ∼0.52 nm. The selected-area electron diffraction pattern (SAED) in Figure 1(d), which was taken from multiple nanoparticles, shows that the ZnO nanoparticles were a polycrystalline wurtzite structure. In contrast, after precursor B was irradiated by a UV-light decomposition process for 5 min, the product's morphology exhibited 1D nanowires, as shown in Figure 1(e) and its inset image of the upper right-hand side. The diameter of the ZnO nanowires is sized between 80 and 200 nm. Figure 1(f) shows that the UV-decomposition process has successfully synthesized the nanowires with high transparency ∼80% (see the inset image of Figure 1(f)) on a PET substrate. This demonstrates that the UV-decomposition can effectively decompose the precursors into the nanowires/nanoparticles on the surface of the PET substrate.

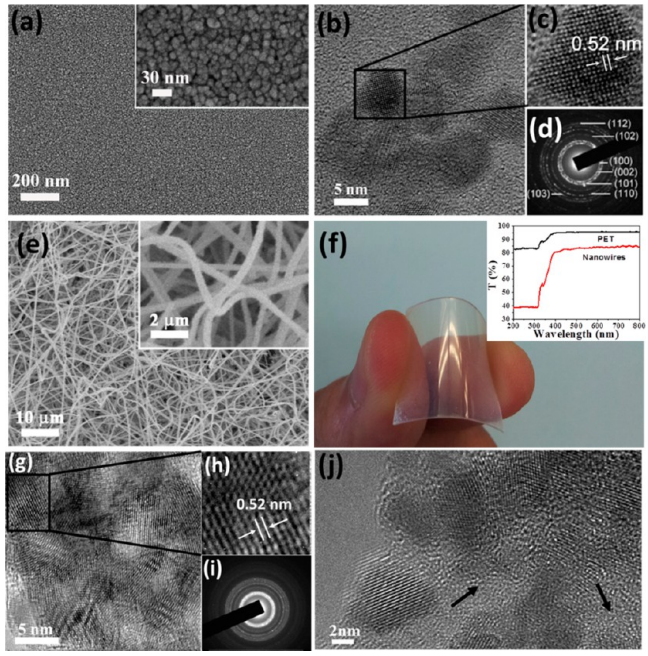

Figure 1. (a) FESEM image of ZnO nanoparticles; inset upper right-hand side: high magnitude SEM image showing the nanoparticles less than 30 nm. (b) TEM image shows the nanoparticles consisted of ultrafine nanoparticles with the size ∼5−10 nm. (c) HRTEM image showing the lattice fringe ∼0.52 nm, which corresponds to the (0001) plane. (d) The SAED pattern reveals the ZnO nanoparticles belong to wurtzite structure. (e) FESEM image of ZnO nanowires; inset upper right-hand side: high magnitude SEM image shows the nanowires with high surface to volume ratio. (f) Nanowires were synthesized on a PET substrate with a high transparency. The inset image revealed the transparency of the nanowires/PET substrate was ∼80%. (g)The TEM image shows the nanowires also consisted of ultrafine nanoparticles, and the (h) HRTEM image shows the lattice fringe ∼0.52 nm, which corresponds to the (0001) plane. (i) The SAED pattern of the ZnO nanowires shows the crystallinity levels (sample B) were poorer than those of the nanoparticles (sample A). (j) In the nanowires (in early growing stage of 3 min), the nanocrystals were deposited by an amorphous layer.

The TEM images in Figure 1(g) and 1(h) show that the nanowires (sample B) consisted of fine single-crystal nanoparticles with lattice fringes of ∼0.52 nm. The concentric circle indicates that the crystallinity of the ZnO nanoparticles (sample A in Figure 1(d)) was superior to that of the ZnO nanowires (sample B in Figure 1(i)). Figure 1(j) further shows that the ZnO nanowires consisted of ultrafine nanoparticles and were covered by an amorphous layer in the early stage (3 min) (see black arrowheads), which was implanted on the surfaces of the nanoparticles. On the basis of our previous works, the amorphous layer can be attributed to zinc hydroxide (i.e., $Zn(OH)_2$).[7]

To investigate relationships between the decomposition time and crystal structure, the precursors A and B were irradiated under UV-light for periods of 3, 5, and 10 min. The powder X-ray diffractograms of the A-series and B-series samples are shown in Figures 2(a) and 2(b). The size-broadened reflections from hexagonal wurtzite-type ZnO had lattice constants of $a = 0.325$ nm and $c = 0.52$ nm (JCPDS 36-1451). Although the B-series samples still exhibited a single phase of wurtzite ZnO, B-series crystallinity levels were generally poorer than those of the A-series samples. The average particle sizes were quantitatively

dx.doi.org/10.1021/am404532q | ACS Appl. Mater. Interfaces 2014, 6, 487−494

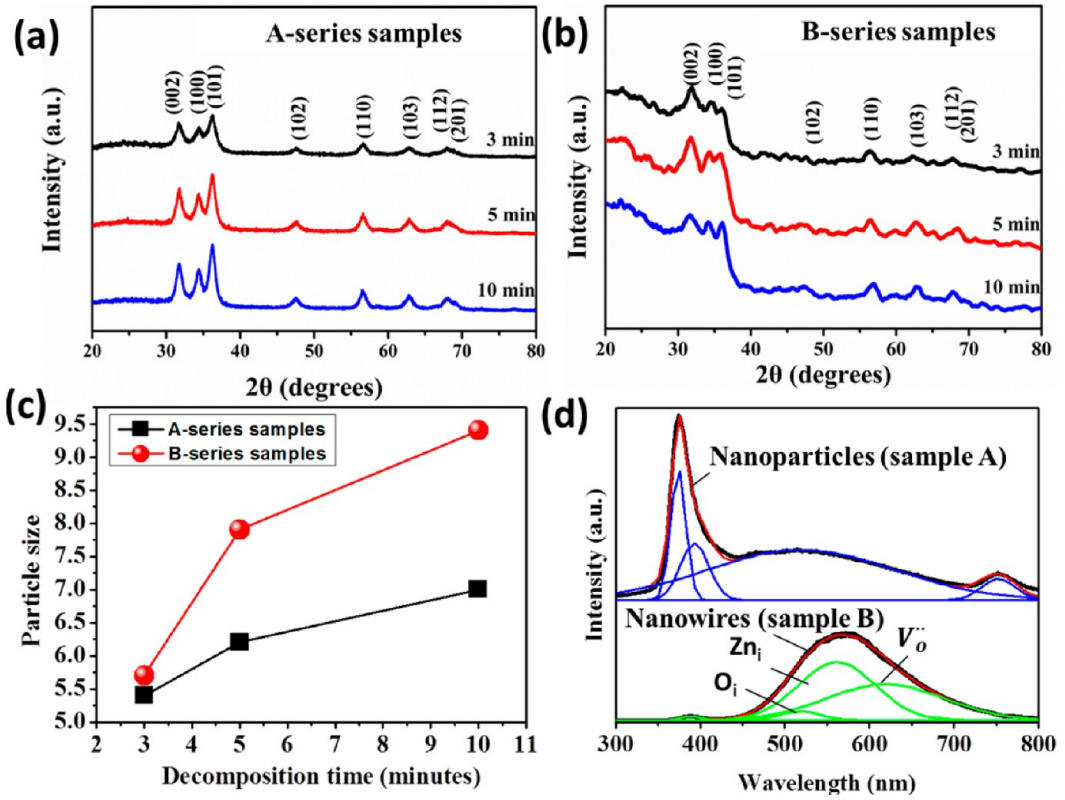

Figure 2. XRD patterns of (a) A-series samples and (b) B-series samples. (c) Shows the average particle size as a function of decomposition time in A- and B-series samples. (d) CL spectra of sample A and sample B, and the sample B (nanowires) shows a high intensity of oxygen vacancy emission band position at a visible wavelength interval.

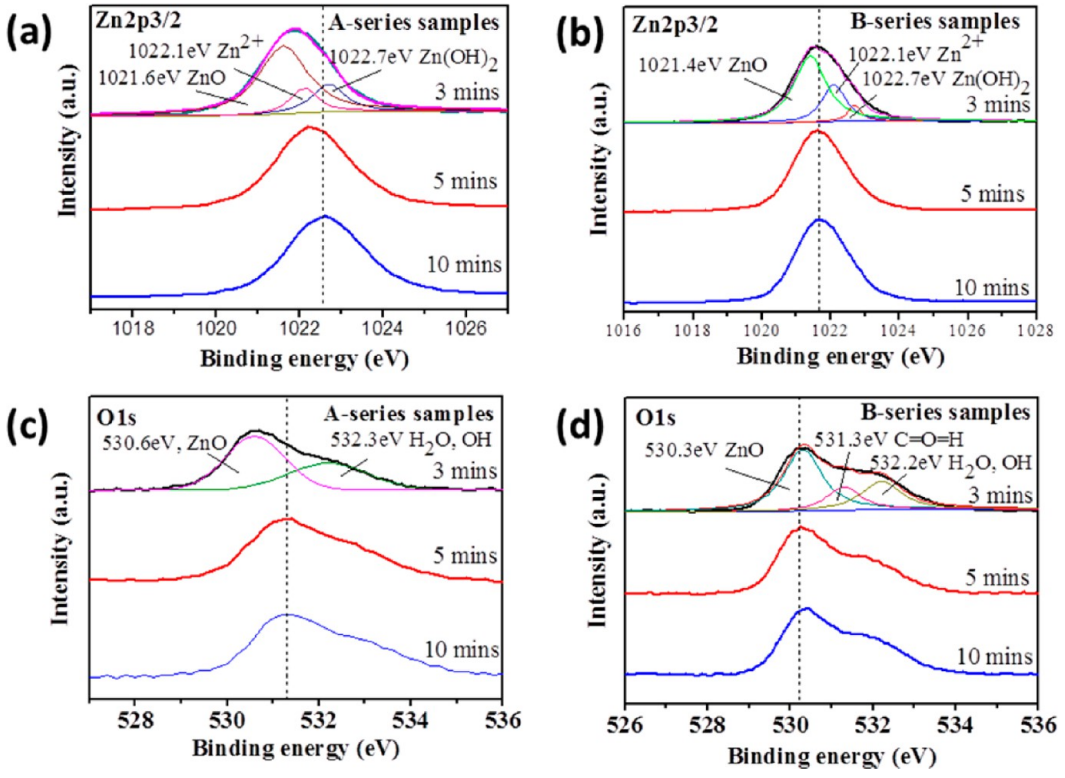

Figure 3. XPS spectra of (a) A-series samples: Zn 2p3/2, (b) B-series samples: Zn 2p3/2, (c) A-series samples: O 1s, and (d) B-series samples: O 1s.

evaluated using the Debye−Scherrer formula,[13] as given in eq 1, where λ is the X-ray wavelength (Cu K_α radiation, 0.15406 nm), 0.9 represents the Debye−Scherrer constant, δ is the full width at half maximum, and θ is the Bragg angle. The evaluated

dx.doi.org/10.1021/am404532q | ACS Appl. Mater. Interfaces 2014, 6, 487−494

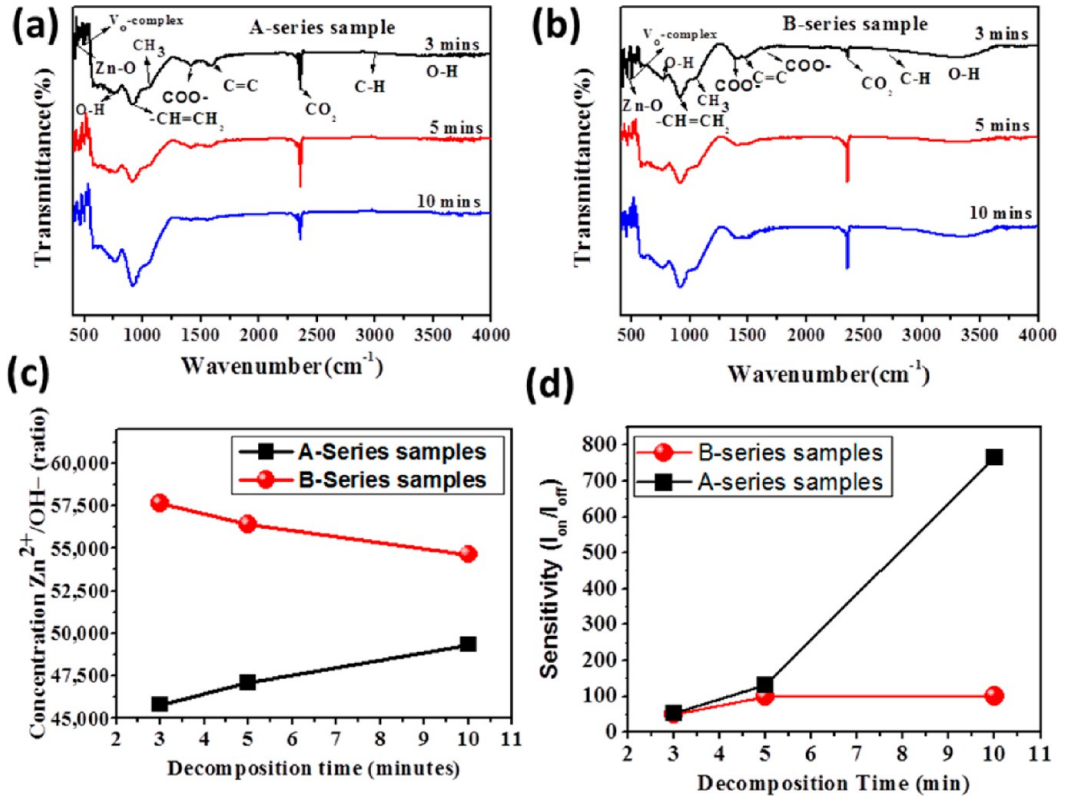

Figure 4. FTIR spectra of (a) A-series samples and (b) B-series samples show a high concentration of hydroxyl (−OH) groups. (c) The concentration of the Zn^{2+}/OH^{-} ratio is a function of decomposition time. (d) The sensitivity as a function of decomposition time is shown in the A- and B-series samples.

average particle sizes of A-series and B-series samples are given in Figure 2(c). Samples subjected to longer decomposition times tended to have larger particle sizes. The average particle size of the A-series samples was smaller than that of the B-series samples. On the basis of the Scherrer line width analysis of all the shown peaks, the particle size was estimated to be ∼6−10 nm. This result was generally consistent with our observation of the TEM images.

$$D = \frac{0.9\lambda}{\delta \cos \theta} \quad (1)$$

In determining the surface state of nanoparticles and nanowires by cathodoluminescence (CL), we investigated A- and B-series samples that had been prepared for a decomposition time of 5 min. As shown in Figure 2(d), in contrast to that of sample A (nanoparticles), the CL spectrum of sample B (nanowires) exhibited a high-intensity emission in a broad visible wavelength interval. Moreover, both sample A and sample B had a near-band-edge emission peak at 382 nm. The broad emission band in the visible region for sample A and sample B can be ascribed to the superposition of green and yellow emissions.[14] An observation of 761 nm was attributed to the second harmonic emission. Sample A showed a stronger intensity than sample B in the UV emission band. It is worth noting that the broad emission band in the visible region in sample B was stronger than that of sample A. The broad emission band was further deconvoluted into three main peaks, namely, 372, 404, and 521 nm, all of which can be regarded as near-band-edge emissions of defect states. These three defect states can be attributed to the presence of zinc hydroxide $Zn(OH)_2$ layers that were positioned on the surface of ZnO nanocrystallites;[7] these three defects formed oxygen interstitial vacancies (O_i), single charge zinc interstitial vacancies (Zn_i), and oxygen vacancies ($V_o^{\cdot\cdot}$,V_o), respectively.[14] On the basis of HRTEM images and the corresponding CL spectra, we therefore propose that the concentrations of zinc hydroxide species in sample B were higher than that of sample A (see discussion below).

To investigate the chemical reaction process, XPS was used to measure the surface states of ZnO nanoparticles/nanowires during the formation processes. The precursors A and B were irradiated by UV-light for 3, 5, and 10 min. The Zn 2p3/2 core-level spectra are given in Figures 3(a) and 3(b). The Zn 2p3/2 peaks were deconvoluted into 1021.6 eV for ZnO and 1022.1 eV for Zn^{2+} and 1022.7 eV for $Zn(OH)_2$.[15] It should be noted that the binding energy of the Zn 2p3/2 peak is located at 1022.0 eV for ZnO nanoparticles because its crystals' sizes were larger than 200 nm.[16] The smaller the particle is, the smaller the binding energy shift effect is. Thus, owing to the size effect,[8,16] we found that a significantly downward shift of binding energy (BE) occurred in the Zn 2p3/2 spectra of A-series samples (see Figure 3(a)) if compared with B-series samples (see Figure 3(b)). When compared with the other samples, the A-series samples exposed for 3 min had the smallest particles; therefore, the Zn 2p3/2 peak was significantly positioned at the lowest bonding energy. Accordingly, the XPS investigation demonstrated that the longer the decomposition time was, the bigger the average particle was. For the B-series samples, Figure 3(b) shows that the Zn 2p3/2 peak did not significantly shift to a low bonding energy. This can be attributed to the fact that the average particle sizes of the B-series samples were larger than those of A-series samples, and BE peaks did not significantly

dx.doi.org/10.1021/am404532q | ACS Appl. Mater. Interfaces 2014, 6, 487−494

shift due to low bonding energy. Figure 3(c) illustrates that each O 1s peak found in any A-series sample can be deconvoluted into two peaks at 530.6 and 532.3 eV, which correspond to the ZnO and weak H_2O peaks, respectively.[17,18] In contrast, Figure 3(d) shows that each O 1s peak found in any B-series sample can be deconvoluted into three peaks at 530.3, 531.3, and 532.2 eV, which correspond to the ZnO, C═O═H bond, and OH (detailed discussion in FTIR below) peaks, respectively.[8,19] The shifting effect of low binding energy was also observed in O 1s peaks in A-series samples (see Figure 3(c)). Thus, for small particles, especially in A-series samples, the low BE peaks obviously shift.

Figure 3(d) is particularly noteworthy. The O 1s peaks in B-series samples still slightly exhibited shift effects to low binding energy. These shift effects can be attributed to the oxygen vacancies produced by the reduction of charge transfer from zinc to oxygen. This tended to increase the shielding effect of the valence electrons in Zn ions.[20] Our CL spectra indicate that the B-series samples possessed a high defect level at the visible emission band (see Figure 2(d)). Therefore, the B-series samples exhibited a higher concentration of oxygen vacancies, and the O 1s peaks were slightly shifted toward lower binding energy levels in B-series samples.

In our XPS results, A- and B-series samples showed broad bands of O 1s spectra at 532.3 eV, which can be assigned to C═O═H or OH species. Fourier transform infrared spectroscopy (FTIR) was performed to further confirm the existence of these chemical bonds. As shown in Figures 4(a) and 4(b), a broad band at 3500 cm^{-1} is assigned to the O−H stretching mode of the hydroxyl group. Peaks between 2830 and 3000 cm^{-1} can be regarded as a C−H stretching vibration of alkane groups. On the basis of FTIR and XPS investigation, after adding water molecules to the $Zn(AcAc)_2$ precursor (e.g., precursor B), the carboxylate (COO−), CO, and hydroxyl (−OH) groups were significantly increased in B-series samples (see Figure 4(b)). In contrast, Figure 4(a) shows that A-series samples exhibited fewer −OH groups than B-series samples. This implies that, during the reaction processes, high concentrations of OH groups were formed in the B-series samples, but similar OH groups were not concentrated in A-series samples.

Formation Mechanism of Nanowires/Nanoparticles. An interesting observation is that the A-series samples formed 0D nanoparticles, while the B-series sample displayed 1D nanowires (see FESEM images in Figure 1(a) and 1(e)). The following reactions were performed to investigate the reaction processes. During decomposition, A-series samples underwent chemical reactions as given by reactions 2−4, while B-series samples were governed by reactions 5−8. The dissociation of $Zn(AcAc)_2$ precursors under UV-light produced $Zn(OH)_2$, which further formed Zn and OH ions (see reaction 2). The UV irradiation of ZnO resulted in the separation of electrons and holes (see reaction 3), which caused oxygen to form oxygen ions that adsorbed on the surface of the nanoparticles. Reaction 4 shows that when the oxygen ions are combined with Zn^{2+} they form ZnO nanoparticles. This is the nanoparticle formation process for A-series samples.

Equations 5−8 explain the chemical reactions of the B-series samples. Equation 5 reveals that when $Zn(AcAc)_2$ was added to water molecules $Zn(OH)_2$ formed with a high concentration of OH species (as shown in XPS, TEM, and CL data). This is because water molecules were added to the $Zn(AcAc)_2$ precursor, which exhibited a ligand exchange reaction between $AcAc^-$ and OH^- in the $Zn(AcAc)_2$-containing solution. The $Zn(OH)_2$ reacted with high concentration of OH species to produce the $Zn[(OH)_4]^{2-}$ species (see eq 6).[21] The $Zn[(OH)_4]^{2-}$ may dissociate into the Zn^{2+} and hydroxyl (OH) ions, which further reacted with each other to form ZnO nanocrystals, and water molecules were then formed (see eq 7). However, the $Zn[(OH)_4]^{2-}$ ions were dissociated into ZnO_2^{-2} and H_2O (as shown by eq 8), and the ZnO_2^{-2} and $Zn[(OH)_4]^{2-}$ ions make an anisotropic growth of ZnO along the [0001] direction with H_2O molecular.[22] In brief, eqs 5−8 explain how water molecules fit into the chain reaction. If there is a high concentration of water molecules, many OH groups may implant on the surface of the nanocrystals. Thus, the residual Zn^{2+} with oxygen vacancies may implant a number of defects on the surfaces of the ZnO nanocrystals. Thus, the CL spectrum of nanowires reveals a high intensity defect band on visible-light emission, but the CL spectrum of nanoparticles does not (see CL image in Figure 2(d)).

$$Zn(OH)_2 \rightarrow Zn^{2+} + 2OH^- \quad (2)$$

$$h\nu \rightarrow e^- + h^+ \quad (3)$$

$$Zn^{2+} + O^{2-} \rightarrow ZnO \quad (4)$$

$$Zn(C_5H_7O_2)_{2(s)}\cdot 2H_2O \rightarrow Zn(OH)_2 + 2C_5H_8O_{2(g)} \quad (5)$$

$$Zn(OH)_2 + 2OH^- \rightarrow Zn(OH)_4^{2-} \quad (6)$$

$$Zn^{2+} + 2OH^- \rightarrow ZnO + H_2O \quad (7)$$

$$Zn(OH)_4^{2-} \rightarrow ZnO_2^{2-} + 2H_2O \quad (8)$$

To demonstrate the ratios of Zn^{2+}/OH^- in the A- and B-series samples, XPS was employed to semi-quantitatively identify the ratio of Zn^{2+}/OH^- as a function of decomposition time. Using Gaussian fitting approximations of the Zn 2p3/2 and O 1s spectra, the ratios of Zn^{2+} and OH^- were calculated by integrating the curves of Zn^{2+} and OH^-, respectively. As shown in Figure 4c, the average ratio of Zn^{2+}/OH^- in the B-series samples was higher than that of the A-series samples. Therefore, we suggest the addition of water molecules to the $Zn(AcAc)_2$ precursor in the B-series samples facilitated the ligand exchange reaction between $AcAc^-$ and OH^- in the $Zn(AcAc)_2$-containing solution and thus formed high concentrations of $Zn(OH)_2$ with OH ions. This explains how the B-series samples possessed high concentrations of $Zn(OH)_2$ and OH peaks compared to the A-series samples, as shown by FTIR and XPS. To reveal the photoresponsive properties, each sample in A- and B-series was irradiated by a UV-lamp with a wavelength of 365−380 nm (intensity ∼ 2.33 mW cm^{-2}).[23] The sensitivity of each sample, S, was defined as $I_{UV\text{-}on}/I_{UV\text{-}off}$[24,25] as shown in Figure 4(d). As the decomposition time increased, the sensitivity increased. The highest sensitivity ratio in this work was that of the B-series sample with 10 min UV-decomposition; its sensitivity ratio was 80 900%.

On the basis of the XPS and FTIR results, in the dissociated $Zn(AcAc)_2$-containing water solution, the $Zn(OH)_2$ further reacted with highly concentrated hydroxyl ions (OH^-) to form $Zn[(OH)_4]^{2-}$, as mentioned by eq 6. Thus, the more water molecules the precursor had, the more OH^- and $Zn[(OH)_4]^{2-}$ it put out. In this work, the B-series samples possessed more water molecules than the A-series samples. Thus, the B-series samples had more OH^- that reacted with $Zn(OH)_2$ to form

dx.doi.org/10.1021/am404532q | ACS Appl. Mater. Interfaces 2014, 6, 487−494

$Zn[(OH)_4]^{2-}$. These species of $Zn[(OH)_4]^{2-}$ fit well with the (0001) polyhedral surface of the ZnO nanocrystals; the spatial resonance encouraged growth in the direction of the *c*-axis,[26] as shown by the schematic diagram in Figure 5. Although

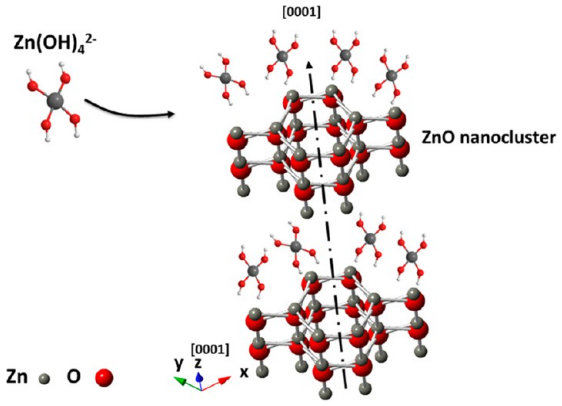

Figure 5. Growth mechanisms of ZnO nanowires. The growth process is facilitated by the tetrahedral structure of the $Zn[(OH)_4]^{2-}$ which fits well with the polyhedral surface (0001). This increases the growth in the [0001] direction more than in other faces.

dissociated $Zn[(OH)_4]^{2-}$ may have formed the Zn^{2+} that reacted with the O^{2-} to form ZnO nanocrystals, the high concentration of hydroxyl ions and H_2O in precursor B provided plenty of opportunities to make Zn^{2+} react with OH^- to form $Zn[(OH)_4]^{2-}$. Subsequently, the elongation of nanopartcles was along the *c*-axis because the most thermodynamically stable plane of (0001) was along the *c*-axis.

To investigate the nanowires' formation process, we sampled the B-series samples with different decomposition times (i.e., 3 and 30 min). Figure 6(a) shows that, for the B samples at 3 min, the particles were fused together, and the lattice planes were aligned relative to each other. The high magnitude TEM image of Figure 6(b) shows that the small particles conglomerated together with a common crystallographic orientation. The dashed line indicates the boundaries at which there was misorientation between the primary particles. The sizes of the assembling units were mostly 5−8 nm,[27] so the primary particles were almost equal in size. Twin boundaries formed between two nanocrystals. Figure 6(c) shows that at 30 min the particle was even more elongated along the [0001] axis.[26] Black arrows indicate boundaries in which some slight misorientations between primary particles have been incorporated.[21] Figure 6(d) further demonstrates oriented aggregation and a coarsening process whereby primary particles irreversibly attach to one another in slightly oriented fashion to produce secondary particles.[28]

A schematic diagram of nanowire formation by oriented attachment is shown in Figure 6(e). The growths from individual particles were crystallographically oriented and partially fused together. As decomposition time increased, the crystallinity increased, and primary particles were free to rotate into an orientation that achieved structural accord at the interface. This is because the nanoparticles possessed high surface energy, which caused quasi-spherical particles to aggregate together to reduce their free energy by consuming the local ions of $Zn[(OH)_4]^{2-}$ species into wire-like structures. This explains how nanowire formation was dominated by the concentration ratios of Zn^{2+}/OH^- and how the amorphous layers of zinc hydroxide were implanted on surfaces of the ZnO

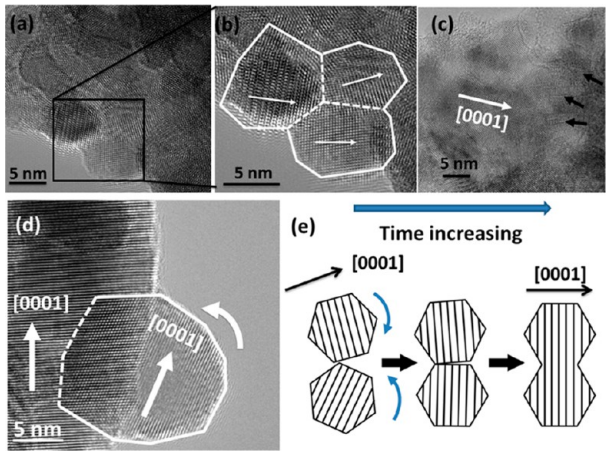

Figure 6. (a) HRTEM image showing the ZnO nanowires at initial growing stage of 3 min. (b) The HRTEM image shows a crystal constructed from at least three primary building block crystallites. The white dash lines highlight the misorientation between three regions of the assembled nanocrystals. (c) After 30 min of decomposition time, the elongation of nanoparticles along the [0001] direction is more significant. (d) One nanocrystal is fused to another larger nanocrystal during the crystal growth process. The larger nanocrystals are constructed by smaller attached nanocrystals with sizes equal to primary particles (5−8 nm). (e) Schematic diagram depicting the growth of nanocrystals by an oriented attachment: two primary particles collide and coalesce in the same crystallographic orientation of [0001], which is the most thermodynamically stable direction in ZnO.

nanocrystals. We suggest that $Zn[(OH)_4]^{2-}$ and $Zn(OH)_2$ species formed on the surfaces of the ZnO nanocrystals. Accordingly, as the formation ratio of ZnO nanocrystals increased, the H_2O increased. This indicates how high concentrations of hydroxyl ions tended to form nanowire morphologies instead of nanoparticles. This is the key component in production of 1D nanowires. Those nanowires were governed by the oriented attachment mechanism.[8,10,11]

In contrast, when water molecules were not added to the precursor of $Zn(AcAc)_2$ in A-series samples, the dominated species was Zn^{2+}, which reacted with oxygen in ambient air to form ZnO nanoparticles. In other words, the precursor of $Zn(AcAc)_2$ provided a much lower concentration of hydroxyl ions and H_2O species during the decomposition process; therefore, there were lower levels of $Zn[(OH)_4]^{2-}$ species in the A samples than in the B samples. The lower concentrations of $Zn[(OH)_4]^{2-}$ offered fewer opportunities for particles to adsorb the $Zn[(OH)_4]^{2-}$ on the (0001) polyhedral surfaces of ZnO nanocrystals. Therefore, the morphology exhibited 0D nanoparticles.

Accordingly, due to the lack of OH species, the ZnO nanoclusters did not have enough driving force to undergo an oriented aggregation. In other words, the H_2O acted as a catalytic enhancement on the self-reaction by undergoing the oriented aggregation mechanism; that oriented aggregation facilitated 1D nanowires under the most thermodynamic favorable conditions. Therefore, if the reaction used the precursor of $Zn(AcAc)_2$ without any additional water molecules, the ZnO took the form of fine nanoparticles, which were randomly distributed throughout the substrate.

Defect State of ZnO on Photoresponsive Properties. Generally, the ultrafine nanoparticles contribute to large surface-to-volume ratios and provided superior sensing

dx.doi.org/10.1021/am404532q | ACS Appl. Mater. Interfaces 2014, 6, 487−494

performance through gas adsorption and desorption mechanisms.[8] However, Figure 4(d) shows that with the increase of the UV decomposition time the particle size and the sensitivity dramatically increased. We suggest that the sensitivity was not directly correlated with the particle size because there were other more important factors that determined the sensing activities.

The CL spectra show that with 5 min UV-decomposition time B-series samples had higher intensity than A-series samples in the range of 450−700 nm. This is because $Zn(OH)_2$ and $Zn[(OH)_4]^{2-}$ implanted on the nanoparticles and had a high surface-area-to-volume ratio defect state. These defect states normally are positioned on the surface of the ZnO nanostructures.[6,29] Figure 7(a) shows the crystallography of

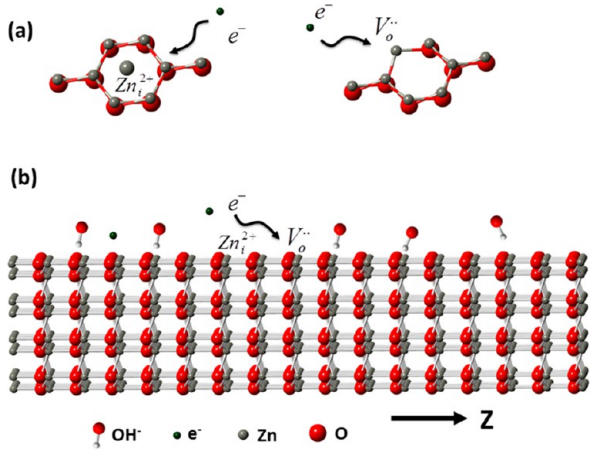

Figure 7. (a) Crystal structure of the ZnO defect states (see details in text). (b) The crystallographic structure of ZnO with the OH^- group and oxygen vacancies, which act as the electron-trapping centers.

these defects such as single charge zinc interstitial (Zn_i)[30] and oxygen vacancies $(V_o^{\cdot\cdot},V_o)$,[31] trapped electrons to recombine with oxygen or hydroxide from ion states (i.e., O^-, OH^-) and to reduce the carrier transfer process. As the UV-decomposition time increased, the defect levels (i.e., oxygen vacancies) dramatically decreased by consuming the $Zn(OH)_2$ and $Zn[(OH)_4]^{2-}$ located on the surface of ZnO nanoparticles to form ZnO nanoclusters. It should be noted that water adsorptions can be dissociated in oxygen vacancies and through proton transfer to a neighboring bridging oxygen atom that forms two bridging OH groups per initial vacancy (see Figure 7(b)).[3,32] Therefore, the oxygen vacancies were effectively decreased by consuming the water molecules. Here, the oxygen defects served as trapping centers for the photogenerated electrons; the defects reduced the charging and discharging of oxygen on the surfaces of the nanoparticles, resulting in poor sensing performance.[7] The crystallinity showed that the longer the UV-decomposition treatment time was, the higher the crystallinity was. Materials that had ZnO with high crystallinity also had a highly efficient electron−hole pair separation ratio. These materials performed an effective photosensing process. This high-crystallinity ZnO nanoparticle mechanism therefore explains how A-series samples possessed an excellent sensing property but B-series samples did not.

4. CONCLUSION

We demonstrated the use of UV radiation on precursor $Zn(AcAc)_2$ and $Zn(AcAc)_2{\cdot}H_2O$ to synthesize ZnO nanoparticles and nanowires on a flexible PET substrate, respectively, under ambient air. The ZnO nanoparticles exhibited a remarkable photocurrent−dark current ratio of ~80 900%, which was 8.5 times that of the ZnO nanowires. We used transmission electron microscopy, X-ray photoelectron spectroscopy, cathodoluminescence spectra, and Fourier transform infrared spectroscopy to discover that the ZnO nanowires possessed many surface properties such as oxygen vacancies and interstitial Zn, hydroxyl, and hydroxide, which acted as key components in the photoresponsive properties and formation processes. The high concentrations of hydroxyl ions and H_2O provided plenty of opportunities to make Zn^{2+} react with OH^- to form $Zn[(OH)_4]^{2-}$, which was the key component that facilitated the formation of one-dimensional nanowires. This work revealed that water molecules played a critical role in the surface defect states, affecting the morphology and the photoresponsive properties of the nanoparticles and nanowires. To the best of our knowledge, this is the first systematic and comprehensive experimental study on the photoresponsive performance, formation mechanisms, and surface chemistry of ZnO nanoparticles and nanowires.

AUTHOR INFORMATION

Corresponding Author

*E-mail: wujm@mx.nthu.edu.tw.

Notes

The authors declare no competing financial interest.

ACKNOWLEDGMENTS

The authors would like to thank the National Science Council of Taiwan, Republic of China, for financially supporting this research under Contract No. NSC 100-2628-E-035-006-MY2; NSC 102-2221-E-035-059-MY3; NSC 102-2221-E-007-146-MY3.

REFERENCES

(1) Huang, M. H.; Mao, S.; Feick, H.; Yan, H. Q.; Wu, Y. Y.; Kind, H.; Weber, E.; Russo, R.; Yang, P. D. *Science* **2001**, *292*, 1897−1899.
(2) Zhu, Z. T.; Zhang, L. F.; Howe, J. Y.; Liao, Y. L.; Speidel, J. T.; Smith, S.; Fong, H. *Chem. Commun.* **2009**, 2568−2570.
(3) Kim, J. Y.; Jeong, H.; Jang, D. J. *J. Nanopart. Res.* **2011**, *13*, 6699−6706.
(4) Ku, C. H.; Wu, J. J. *Appl. Phys. Lett.* **2007**, *91*, 093117.
(5) Wang, Z. L.; Song, J. H. *Science* **2006**, *312*, 242−246.
(6) Li, D.; Leung, Y. H.; Djurisic, A. B.; Liu, Z. T.; Xie, M. H.; Shi, S. L.; Xu, S. J.; Chan, W. K. *Appl. Phys. Lett.* **2004**, *85*, 1601−1603.
(7) Wu, J. M.; Chen, Y. R. *J. Phys. Chem. C* **2011**, *115*, 2235−2243.
(8) Beneventi, P.; Capelletti, R.; Kovacs, L.; Peter, A.; Manotti, A. M. L.; Ugozzoli, F. *J. Phys.: Condens. Matter* **1994**, *6*, 6329−6344.
(9) Iwasaki, M.; Inubushi, Y.; Ito, S. *J. Mater. Sci. Lett.* **1997**, *16*, 1503−1505.
(10) Penn, R. L.; Banfield, J. F. *Science* **1998**, *281*, 969−971.
(11) Penn, R. L. *J. Phys. Chem. B* **2004**, *108*, 12707−12712.
(12) Wu, J. M.; Chen, Y. R.; Lin, Y. H. *Nanoscale* **2011**, *3*, 1053−1058.
(13) Patterson, A. L. *Phys. Rev.* **1939**, *56*, 978−982.
(14) Djurisic, A. B.; Leung, Y. H. *Small* **2006**, *2*, 944−961.
(15) Dake, L. S.; Baer, D. R.; Zachara, J. M. *Surf. Interface Anal.* **1989**, *14*, 71−75.
(16) Tay, Y. Y.; Li, S.; Sun, C. Q.; Chen, P. *Appl. Phys. Lett.* **2006**, *88*, 178118.
(17) Martensson, N.; Malmquist, P. A.; Svensson, S.; Basilier, E.; Pireaux, J. J.; Gelius, U.; Siegbahn, K. *Nouv. J. Chim.* **1977**, *1*, 191−195.
(18) Nefedov, V. I.; Firsov, M. N.; Shaplygin, I. S. *J. Electron. Spectrosc.* **1982**, *26*, 65−78.

(19) Stoyanov, P.; Akhter, S.; White, J. M. *Surf. Interface Anal.* **1990**, *15*, 7.
(20) Barr, T. L.; Shikha Varma, M. Y. *J. Vac. Sci. Technol. A* **1992**, *10*, 2383.
(21) Cheng, B.; Shi, W. S.; Russell-Tanner, J. M.; Zhang, L.; Samulski, E. T. *Inorg. Chem.* **2006**, *45*, 1208−1214.
(22) Dem'yanets, L. N.; Kostomarov, D. V.; Kuz-mina, I. P. *Inorg. Mater.* **2002**, *38*, 124−131.
(23) Wu, J. M.; Kuo, C. H. *Thin Solid Films* **2009**, *517*, 3870−3873.
(24) Wu, J. M.; Hsu, G. K.; Yeh, H. H.; Lin, H. C. *J. Electrochem. Soc.* **2012**, *159*, H497−H501.
(25) Wu, J. M.; Liou, L. B. *J. Mater. Chem.* **2011**, *21*, 5499−5504.
(26) Solis-Pomar, F.; Martinez, E.; Melendrez, M. F.; Perez-Tijerina, E. *Nanoscale Res. Lett.* **2011**, *6*, 524.
(27) Zhang, J.; Wang, Y. H.; Zheng, J. S.; Huang, F.; Chen, D. G.; Lan, Y. Z.; Ren, G. Q.; Lin, Z.; Wang, C. *J. Phys. Chem. B* **2007**, *111*, 1449−1454.
(28) Penn, R. L.; Tanaka, K.; Erbs, J. *J. Cryst. Growth.* **2007**, *309*, 97−102.
(29) Hsu, N. E.; Hung, W. K.; Chen, Y. F. *J. Appl. Phys.* **2004**, *96*, 4671−4673.
(30) Liu, M.; Kitai, A. H.; Mascher, P. *J. Lumin.* **1992**, *54*, 35−42.
(31) Greene, L. E.; Law, M.; Goldberger, J.; Kim, F.; Johnson, J. C.; Zhang, Y. F.; Saykally, R. J.; Yang, P. D. *Angew. Chem. Int., Ed.* **2003**, *42*, 3031−3034.
(32) Schaub, R.; Thostrup, P.; Lopez, N.; Lægsgaard, E.; Stensgaard, I.; Norskov, J. K.; Besenbacher, F. *Phys. Rev. Lett.* **2001**, *87*, 266104.